UCRL-JRNL-204232

Driving Mechanism of SOL Plasma Flow and Effects on the Divertor Performance in JT-60U

N. Asakura, H. Takenaga, S. Sakurai, G.D. Porter, T.D. Rognlien, M.E. Rensink, K. Shimizu, S. Higashijima and H. Kubo

May 2004

Nuclear Fusion

UCRL-JRNL-204232

Driving mechanism of sol plasma flow and effects on the divertor performance in JT-60U

N. Asakura[1], H. Takenaga[1], S. Sakurai[1], G.D. Porter[2], T.D. Rognlien[2], M.E. Rensink[2], K. Shimizu[1], S. Higashijima[1] and H. Kubo[1]

[1] Japan Atomic Energy Research Institute, Naka-machi, Naka-gun, Ibaraki 311-0193, Japan
[2] Lawrence Livermore National Laboratory, PO Box 808, Livermore, CA 94550, USA

E-mail: asakuran@fusion.naka.jaeri.go.jp

Abstract
The measurements of the SOL flow and plasma profiles both at the high-field-side (HFS) and low-field-side (LFS), for the first time, identified the SOL flow pattern and its driving mechanism. 'Flow reversal' was found near the HFS and LFS separatrix of the main plasma for the ion ∇B drift direction towards the divertor. 'Flow reversal' at the main SOL was reproduced numerically using the UEDGE code with the plasma drifts included although Mach numbers in measurements were greater than those obtained numerically. Particle fluxes towards the HFS and LFS divertors produced by the parallel SOL flow and $\boldsymbol{E}_r \times \boldsymbol{B}$ drift flow were evaluated from the measured profiles of Mach numbers, the density and the radial electric field. The drift flux in the private flux region was also evaluated, and it was found that its contribution to the HFS-enhanced asymmetry of the divertor particle flux was larger than the ion flux from the HFS SOL. The ion flux for the intense gas puff and divertor pump ('puff and pump') was investigated, and it was found that both the Mach number and density were enhanced, in particular, at the HFS. Ion flux at the HFS SOL can be enhanced so as to become larger than the drift flux in the private flux region.

PACS numbers: 52.30.-q, 52.55.Fa

(Some figures in this article are in colour only in the electronic version)

1. Introduction

Plasma flow in the scrape-off layer, i.e. SOL flow, is generally produced towards the divertor plates along the magnetic field lines, and it plays an important role in the plasma transport [1]. The parallel SOL flow is expected to increase with an intense gas puff and divertor pump (puff and pump), and enhancement of the *friction force* on the impurity ions can explain the improvement in impurity shielding from the main plasma [2, 3]. On the other hand, the SOL flow away from the low-field-side (LFS) divertor, 'flow reversal' (opposite to what one expects from a simple picture of the plasma flow), has been generally observed near the separatrix of the LFS SOL, in particular, for the ion ∇B drift direction towards the divertor [4–7]. Recently, understanding of the mechanisms producing the 'flow reversal', resulting from the poloidal variation of the plasma drift velocity, has progressed in the toroidal plasma model [8, 9], simulation [10] and experiments [11]. Consequently, components of both drift and parallel flows determine plasma transport in SOL. On the other hand, drift flow in the private flux region plays an important role in plasma transport in the divertor, and it is thought to be a mechanism that produces in–out asymmetry in the divertor particle flux [12, 13]. A quantitative evaluation of the drift effects on the plasma transport in the SOL and divertor should be established in order to control plasma and impurities in magnetic configurations relevant to a tokamak reactor.

Determination of the SOL flow pattern has been done recently in JT-60U experiments. Reciprocating Mach probes were installed at the high-field-side (HFS) baffle, LFS midplane and just below the X-point as shown in figure 1. The SOL flow pattern is shown in section 2. In section 3, experimental results are compared to UEDGE simulations, and the plasma drift effect on the parallel SOL flow is investigated. In section 4, SOL particle fluxes towards the HFS and LFS divertors are evaluated from components of the parallel SOL flow and perpendicular $E_r \times B$ drift flow. The contribution of the $E_r \times B$ drift flow to in–out asymmetry in the ion flux

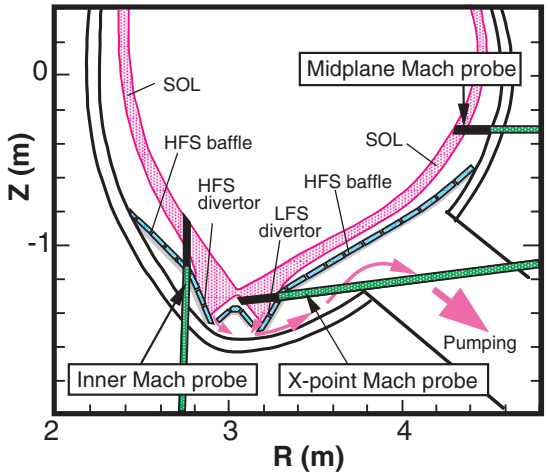

Figure 1. SOL flow and plasma profiles along black lines are measured with three reciprocating Mach probes at the HFS baffle, LFS midplane, and just below X-point.

is investigated. The SOL flow during puff and pump and the influence on the divertor plasma are investigated in section 5. Summary and conclusions are given in section 6.

2. SOL flow measurements at LFS and HFS

The profiles of ion saturation currents at the electron- and ion-drift sides, j_s^{e-s} and j_s^{i-s}, electron temperatures, T_e^{e-s} and T_e^{i-s}, and floating potential, V_f, are measured. The Mach number of the parallel SOL flow is deduced from the ratio of j_s^{e-s} to j_s^{i-s}, using Hutchinson's formula [14]: $M_\parallel = 0.35 \ln(j_s^{e-s}/j_s^{i-s})$, where positive and negative values show the direction towards the LFS and HFS divertors, respectively. The plasma potential, V_p, and radial electric field, E_r, are calculated using a sheath model ($V_p = V_f + 2.75\,T_e$, where higher T_e^{e-s} or T_e^{i-s} is used) and its differentiation. Parameters of the L-mode discharge, $I_p = 1.6$ MA, $B_t = 3.3$ T, $q_{95} = 3.5$ and $P_{NBI} = 4.3$ MW, are fixed. Deuterium plasma and NB are used. The main plasma density, $\bar{n}_e$, is maintained during probe measurements, and it changes from 1.2×10^{19} to 3.9×10^{19} m^{-3} ($\bar{n}_e/n^{GW} = 0.23$–0.73, where $n^{GW} = 5.2 \times 10^{19}$ m^{-3}) on a shot-by-shot basis.

Both $\bar{n}_e$ and the ion ∇B drift direction were found to affect the plasma flow velocity [11, 15]. Profiles of the Mach number at three locations are overlaid in figure 2 for relatively low and high $\bar{n}_e$ (1.6 and 2.4×10^{19} m^{-3}) under the attached divertor condition, where the ion ∇B drift direction is towards the divertor. Three profiles are mapped to the LFS midplane, and the data in the private flux region for the X-point Mach probe is not plotted. For midplane radii (r_{mid}) less than and greater than 4 cm, the field lines are connected to the divertor plate and the baffle, respectively. The SOL flow profile at the LFS midplane shows that 'flow reversal' (SOL flow away from X-point and towards the plasma top) occurs in the wide region ($r_{mid} < 5$ cm), and that the flow reversal gradually decreases at the outer flux surfaces. On the other hand, at the X-point, subsonic flow ($M_\parallel = 0.4$–0.5) towards the divertor is observed. These two facts suggest that stagnation of the parallel SOL flow occurs between the X-point and the LFS midplane.

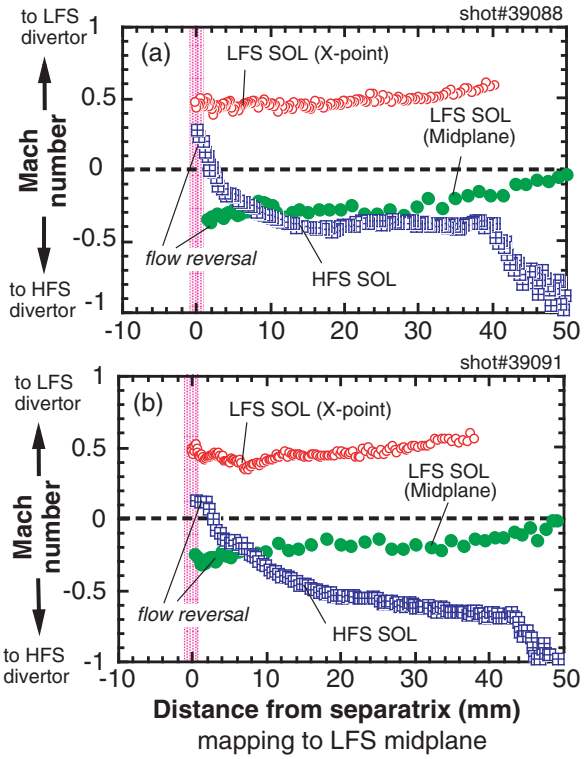

Figure 2. Profiles of Mach numbers measured by reciprocating Mach probes (at the LFS midplane, just below the X-point and above the HFS baffle) for the ion ∇B drift direction towards the divertor: (*a*) $\bar{n}_e = 1.6 \times 10^{19}$ m^{-3} and (*b*) $\bar{n}_e = 2.4 \times 10^{19}$ m^{-3}.

Characteristics of HFS SOL flow change near the separatrix. The SOL flow away from the HFS divertor with $M_\parallel = 0.1$–0.2 is found near the separatrix. The Mach number of the flow reversal is smaller, and it is localized ($r_{mid} < 0.4$ cm) compared to that observed at the LFS midplane ($|M_\parallel| \sim 0.2$–0.3 and $r_{mid} < 5$ cm). At the outer flux surfaces ($1 < r_{mid} < 4$ cm), subsonic SOL flow towards the HFS divertor ($M_\parallel \sim -0.4$) is observed. This fact suggests that stagnations of the SOL flow occur at different poloidal locations for each flux surface: stagnation of the SOL flow near the separatrix ($r_{mid} < 0.4$ cm) occurs downstream from the HFS Mach probe, while stagnations in the outer flux surfaces ($r_{mid} > 0.4$ cm) occur upstream from the Mach probe.

With increasing $\bar{n}_e$, Mach numbers of the flow reversal, both at the HFS and LFS midplane, decrease as shown in figure 2(*b*). On the other hand, $|M_\parallel|$ at the HFS outer flux surfaces increases, whereas the SOL flow profile at LFS below the X-point does not change. The particle flux towards the divertor, $n_i V_\parallel$, which is represented by $n_i M_\parallel C_s$ (C_s is the ion acoustic speed), is enhanced, in particular, at the HFS SOL. In–out asymmetry of the particle flux and influence of the gas puff on the SOL flow are discussed in sections 4 and 5, respectively.

For the ion ∇B drift direction away from the divertor, 'flow reversal' was not observed at the main SOL [15]: stagnation of the SOL flow occurs upstream of the HFS probe and LHS midplane probe, i.e. in the upper half of the main SOL. As a result, one can conclude that an effect of the plasma drifts near the separatrix of the main plasma edge produces the parallel SOL flow against the ∇B drift direction.

3. SOL plasma simulation with drift effects

Classical drifts of $\boldsymbol{E} \times \boldsymbol{B}$ and $\boldsymbol{B} \times \nabla B$ (or diamagnetic for fluid model) have been shown to influence the SOL plasma transport in the torus. For the ion ∇B drift towards the divertor, the parallel SOL flow can be produced away from the divertor both at the HFS and LFS SOLs, due to poloidal asymmetries of the $E_r \times B_t$ and $\nabla p_i \times B_t$ drift velocities [16, 17, 11]. However, radial and poloidal distributions of the SOL flow pattern in the experiments, where plasma and neutral source densities were different for the non-circular plasma configuration and the divertor geometry, could not be investigated in the classical model. The two-dimensional plasma flow pattern was investigated in the plasma and divertor geometries of the JT-60U. Effects such as $\boldsymbol{E} \times \boldsymbol{B}$, $\boldsymbol{B} \times \nabla B$ and diamagnetic drifts have been included in the simulation code of the plasma fluid models, UEDGE [18]. At this stage, the plasma calculation mesh covers the edge and SOL area of $-3 < r_{\mathrm{mid}} < 5$ cm. In this study, constant diffusion coefficients, i.e. $\chi_i = \chi_e = 1\,\mathrm{m^2\,s^{-1}}$ and $D = 0.25\,\mathrm{m^2\,s^{-1}}$, over the SOL area [18] are used since the measured T_e and n_e profiles at the LFS midplane are reproduced in the region $0 < r_{\mathrm{mid}} < 3$ cm.

3.1. Drift effects on parallel SOL flow

Figure 3 shows calculated Mach numbers of the parallel SOL flow as a function of the normalized poloidal distance (d_{pol}) from the HFS target to the LFS target: (a) near the separatrix ($r_{\mathrm{mid}} = 0.2$–0.4 cm) and (b) at the outer flux surface ($r_{\mathrm{mid}} = 1.4$–1.8 cm). Here, the simulation without drift effects is also shown. Simulation results including the drift effects, as shown in figure 3(a), demonstrate that the SOL flow from the X-point to the plasma top is produced at the LFS SOL ($0.36 < d_{\mathrm{pol}} < 0.93$), while the SOL flow towards the LFS divertor is seen just above and below the X-point ($d_{\mathrm{pol}} > 0.93$). Parallel flow towards the plasma top is driven also at the HFS SOL ($0.13 < d_{\mathrm{pol}} < 0.35$), and in–out asymmetry of the 'flow reversal' is seen. This is what we call a small and narrow 'flow reversal' in section 2 although the 'flow reversal' area appears in the simulation slightly upstream from the HFS Mach probe location ($d_{\mathrm{pol}} = 0.11$). In the region above the X-point, the direction of the parallel SOL flow is influenced also by the divertor plasma condition: the parallel SOL flow is generated towards the divertor due to a reduction in T_e at the divertor. For the simulation, T_e values at the HFS SOL and divertor are lower than those in the experiment. Thus, the SOL flow towards the HFS divertor is seen in the main SOL ($0.05 < d_{\mathrm{pol}} < 0.13$). Figure 3($b$) shows that the 'flow reversal' at the outer flux surfaces in the main SOL appears more upstream ($0.23 < d_{\mathrm{pol}} < 0.42$ at HFS, and $0.42 < d_{\mathrm{pol}} < 0.82$ at the LFS) than those near the separatrix. The SOL flow towards the HFS divertor is enhanced at the HFS Mach probe.

As a result, simulation including the drift effects demonstrated that the parallel SOL flow towards the plasma top appears at the main SOL, and that the Mach numbers become maximal at the LFS and HFS midplane. These characteristics of the SOL flow pattern are consistent with measurements at the three Mach probe locations. Simulation results suggest that stagnations of the parallel SOL flow appear at three locations of the main SOL: one is near the plasma top, and others are at the HFS and LFS SOLs just above the X-point.

3.2. SOL flow profiles in simulation and measurement

Radial profiles of the calculated Mach number, $M_{\parallel}^{\mathrm{cal}}$, and the measured one, $M_{\parallel}^{\mathrm{meas}}$, are compared at the Mach probe locations. At the HFS SOL, figure 4(a) shows that $M_{\parallel}^{\mathrm{cal}} \sim 0$

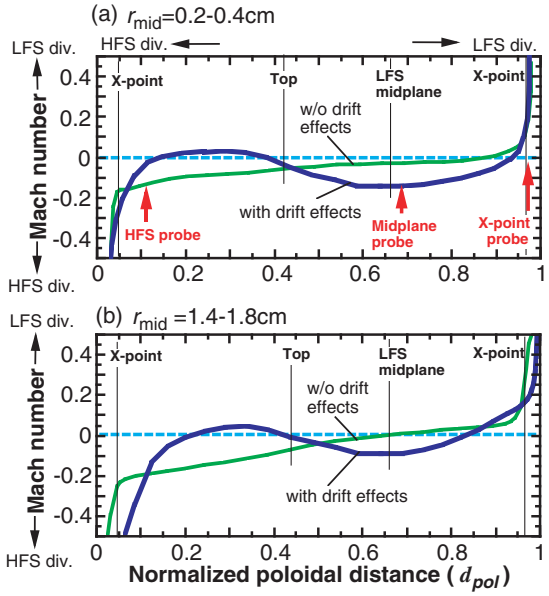

Figure 3. Mach numbers (a) for $r_{\mathrm{mid}} = 0.2$–0.4 cm and (b) for $r_{\mathrm{mid}} = 1.4$–1.8 cm, as a function of normalized poloidal distance from the HFS divertor. Cases with (black lines) and without (grey lines) drift effects included are shown. Mach probe locations are shown by three arrows.

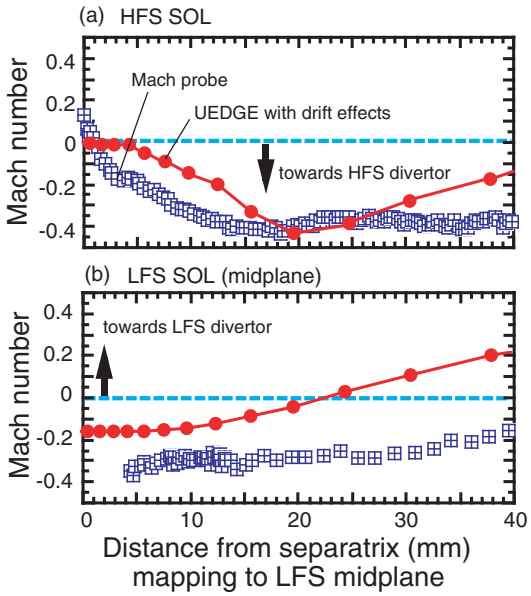

Figure 4. Comparison of calculated (●) and measured (⊞) Mach numbers along the probe axis, (a) above the HFS baffle and (b) at the LFS midplane. Distance from the separatrix is mapped to the LFS midplane.

at the separatrix and $M_{\parallel}^{\rm cal} \sim -0.4$ at $r_{\rm mid} \sim 2$ cm, and that these values are comparable to $M_{\parallel}^{\rm meas}$. However, values of $|M_{\parallel}^{\rm cal}|$ at $0 < r_{\rm mid} < 2$ cm and $r_{\rm mid} > 3$ cm become smaller than $|M_{\parallel}^{\rm meas}|$. At the LFS midplane, figure 4(*b*) shows that the Mach number and width of the calculated 'flow reversal' is small ($|M_{\parallel}^{\rm cal}| \sim 0.2$) and narrow ($\Delta r_{\rm mid} \sim 2.2$ cm) compared to the measurement ($|M_{\parallel}^{\rm meas}| = 0.3$–$0.4$ and $\Delta r_{\rm mid} \sim 5$ cm), although the electron density and temperature profiles are comparable for simulation and measurement.

The above comparative study of the parallel flow profiles in the main SOL indicates that in–out asymmetry of the 'flow reversal' was simulated including the drift effects. However, the 'flow reversal' was small and localized compared to the measurements. The radial profile of the plasma potential and distributions of impurity densities along the field lines were not well reproduced to simulate the experimental electric field, E_r, and the radiation profile in the divertor. Improvement of the modelling of the SOL plasma and impurities as well as inclusion of the drift effects are needed to distinguish the measured profiles of the SOL flow at the HFS and LFS.

4. Particle fluxes towards HFS and LFS divertors

In section 3, we found that the parallel flow pattern in the main SOL was determined by plasma drift effects. However, the magnitude of the drift effects in the present simulation was too small to account for the measurements. In this section, the net particle fluxes towards the HFS and LFS divertors are investigated from the experiments. We evaluate the net particle flux from two components, i.e. the parallel flow, $n_{\rm i}V_{\parallel}(=n_{\rm i}M_{\parallel}C_{\rm s}$, where $C_{\rm s}$ is the ion acoustic speed), and the drift flow, $n_{\rm i}V_{\rm drift}$, using the measurements. Components of $n_{\rm i}V_{\parallel}$ and $n_{\rm i}V_{\rm drift}$ coming from the particle flux in the direction towards the divertor are described as the poloidal components, $n_{\rm i}V_{\parallel}\Theta$ and $n_{\rm i}V_{\rm drift}\Phi$, respectively. Here, $\Theta = B_{\rm p}/B_{\parallel}$ varies in the torus and $\Phi = B_{\rm t}/B_{\parallel}(\sim 1)$. Distributions of the parallel and drift flows upstream of the HFS and LFS divertors are, for the first time, established enabling one to understand the particle transport in the SOL and the divertor. At the same time, large $E_r \times B$ drift flow in the private flux region [12] is evaluated from measurements of the E_r and the $n_{\rm e}$ profiles, and the mechanism of producing the in–out asymmetry in the divertor ion flux is determined.

Positive E_r is generally produced in the main SOL, and the $E_r \times B$ drift flow, $n_{\rm i}V_{\rm drift}^{E\times B}(=n_{\rm i}E_r/B_{\rm t})$, constitutes the particle flux onto the LHS divertor for the ion ∇B drift direction towards the divertor. The diamagnetic flow, $n_{\rm i}V_{\rm drift}^{\rm dia}$, has the same direction, but it does not constitute the particle flux onto the divertor. Thus, the $E_r \times B$ drift flow is considered as the drift flow in this study. Here, the $E_r \times B$ drift flow in the private flux region constitutes the particle flux onto the HFS divertor.

4.1. Parallel SOL flow and E × B drift flow

The poloidal components of the particle flux densities, $n_{\rm i}V_{\parallel}\Theta$ and $n_{\rm i}V_{\rm drift}^{E\times B}\Phi$, are shown in figure 5. Here, we assume $n_{\rm i} = n_{\rm e}$. The drift flow has a positive value, which produces particle fluxes away from the HFS divertor and towards the

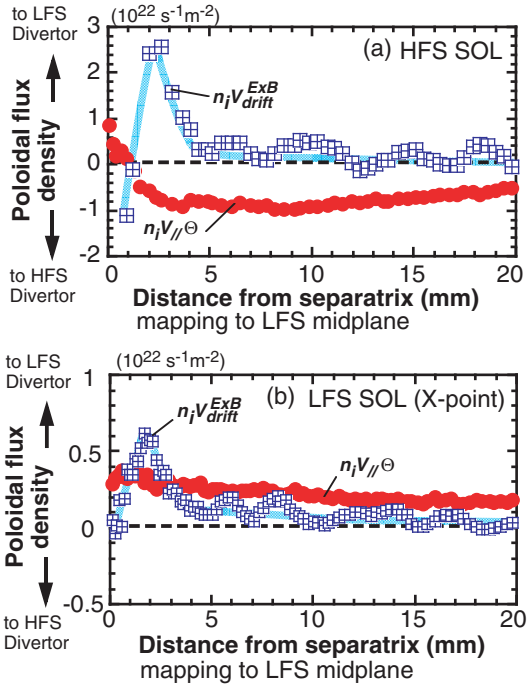

Figure 5. Components of the poloidal flux produced by the parallel SOL flow, $n_{\rm i}V_{\parallel}\Theta$ (●) and $E_r \times B$ drift flow, $n_{\rm i}V_{\rm drift}^{E\times B}$ (⊞) in the common flux region: (*a*) for the HFS SOL and (*b*) for the LFS SOL just below the X-point. Positive and negative values show the flow directions towards the LFS and HFS divertors, respectively. The thick line traces the change of the $E_r \times B$ drift flow.

LFS divertor. At the HFS and LFS, the poloidal flux density of the drift flow is dominant near the separatrix ($r_{\rm mid} < 0.4$ cm). Here, the maximum $n_{\rm i}V_{\rm drift}^{E\times B}\Phi$ of 0.7×10^{22} s^{-1} m^{-2} at the LFS is smaller than the value 2.6×10^{22} s^{-1} m^{-2} at the HFS since E_r near the X-point (4.3 kV m^{-1}) is a factor of 3 smaller than E_r at the HFS SOL (13.5 kV m^{-1}) due to a large magnetic flux expansion factor (7.2) near the X-point compared to 2.1 at the HFS SOL.

The poloidal components of the particle flux density in the private flux region are shown in figure 6(*b*), which is produced by large negative E_r in the private plasma under the attached divertor condition as shown in figure 6(*a*). The $E_r \times B$ drift flux is very large and it contributes to particle transport from the LFS to the HFS divertor.

When the divertor plasma is detached at the LFS divertor target (corresponding to the magnetic flux surfaces of $r_{\rm Xp} <$ 3 cm at the X-point Mach probe), negative E_r appears in the common flux region as shown in figure 6(*a*). The $E_r \times B$ drift produces particle flux away from the LFS divertor as shown in figure 6(*b*). On the other hand, SOL flow increases up to the sonic level towards the ionization front above the target plate [7]: $n_{\rm i}V_{\parallel}\Theta$ increases as shown in figure 6(*c*). The two poloidal components, i.e. $n_{\rm i}V_{\rm drift}^{E\times B}\Phi$ and $n_{\rm i}V_{\parallel}\Theta$, are comparable and in opposite directions; thus the large toroidal flow towards the counter $B_{\rm t}$ (and $I_{\rm p}$) direction is produced upstream of the plasma detachment (at the LFS). At the outer flux surfaces ($r_{\rm Xp} > 3$ cm), the divertor plasma is attached, and large $n_{\rm i}V_{\parallel}\Theta$ is also observed whereas $n_{\rm i}V_{\rm drift}^{E\times B}\Phi$ is small. As a result, the net particle flux towards the divertor increases in the partially detached divertor.

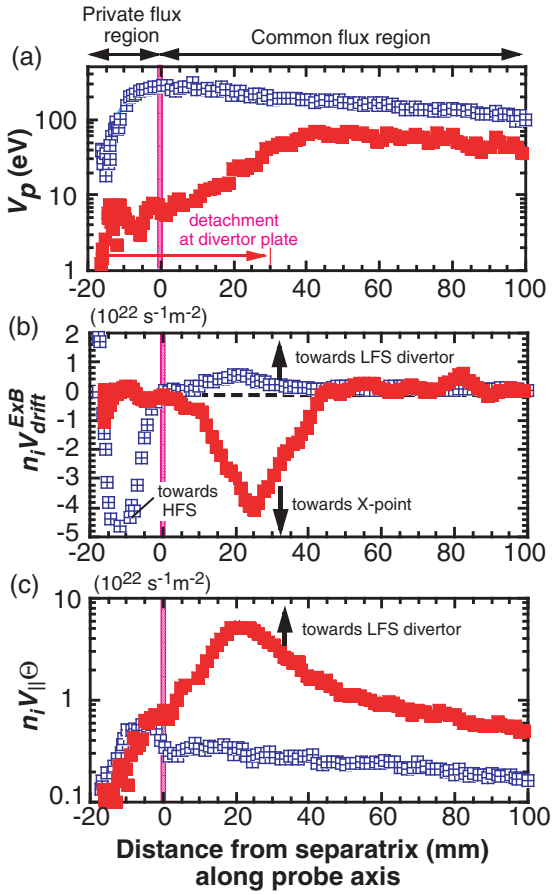

Figure 6. Profiles of (*a*) plasma potential, (*b*) flux density produced by $E_r \times B$ drift, (*c*) poloidal component of parallel flux, as a function of the X-point Mach probe axis. Crosses and closed squares represent profiles under attached and detached (closed squares) divertor conditions, where $\bar{n}_e = 1.6$ and 3.1×10^{19} m^{-3}, respectively. Positive value shows the direction towards the LFS divertor.

4.2. Influence of the E × B drift on particle flux

Influences of the drift flow on total particle fluxes, Γ_p^{HFS} and Γ_p^{LFS}, are investigated. Γ_p^{HFS} and Γ_p^{LFS} are calculated by integrating $n_i V_\parallel \Theta$ and $n_i V_{drift}^{E\times B} \Phi$ across the SOL along the probe scan from the separatrix ($r = 0$) to the outermost radius ($r = r_{div}$), where the field line is connected to the divertor, as follows:

$$\Gamma_p^{HFS/LFS} = \int_0^{r_{div}} 2\pi R n_i [V_\parallel \Theta + V_{drift}^{E\times B} \Phi] \nabla\varphi \cdot dr, \quad (1)$$

where the positive value shows the particle flux towards the LFS divertor. Equation (1) is written as $\Gamma_p^{HFS/LFS} = \Gamma_{p,\parallel}^{HFS/LFS} + \Gamma_{p,drift}^{HFS/LFS}$, where $\Gamma_{p,\parallel}^{HFS}$ and $\Gamma_{p,\parallel}^{LFS}$ have negative and positive values, respectively. Figure 7 shows $|\Gamma_p^{HFS}|$ and Γ_p^{LFS}, and the ratio of the $E_r \times B$ drift flux to parallel flux as a function of $\bar{n}_e/n^{GW}$. Components of the parallel and drift fluxes are shown in table 1 for attached and detached divertors. The total particle flux at the private flux region, Γ_p^{Prv}, is calculated from equation (1), where two components are integrated in the private flux region ($-2 < r_{Xp} < 0$ cm).

At low $\bar{n}_e$, $|\Gamma_{p,\parallel}^{HFS}|$ is larger than $\Gamma_{p,drift}^{HFS}$, i.e. $\Gamma_{p,drift}^{HFS}/|\Gamma_{p,\parallel}^{HFS}|$ is 0.3–0.5. Thus, $\Gamma_p^{HFS} = -(1.5\text{–}2.5) \times 10^{21}$ s^{-1}, and

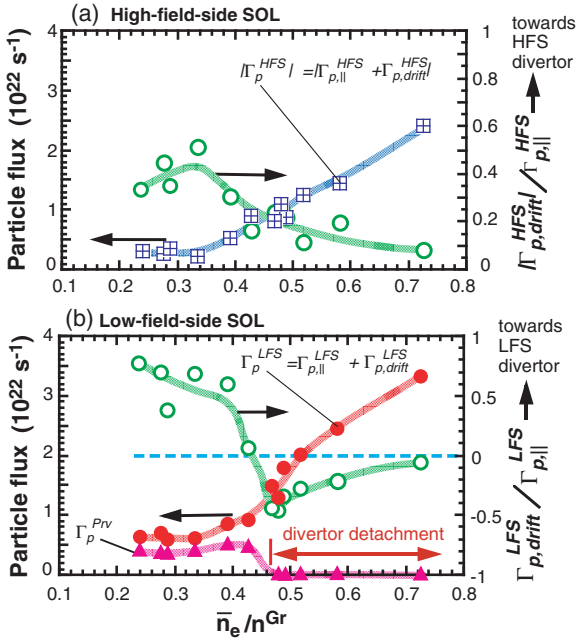

Figure 7. Total poloidal fluxes towards divertors, Γ_p^{HFS} (⊞) and Γ_p^{LFS} (●), and the ratio of the drift flow component to the parallel flow component, $\Gamma_{p,drift}/\Gamma_{p,\parallel}$ (○), as a function of $\bar{n}_e/n^{Gr}$: (*a*) for HFS and (*b*) for LFS just below the X-point. Drift flux from the LFS to the HFS, Γ_p^{Prv}, is also shown by ▲.

the direction of Γ_p^{HFS} is towards the HFS divertor. At the LFS below the X-point, $\Gamma_{p,\parallel}^{LFS}$ is also larger than $\Gamma_{p,drift}^{LFS}$, i.e. $\Gamma_{p,drift}^{LFS}/\Gamma_{p,\parallel}^{LFS}$ is 0.45–0.75; then, $\Gamma_p^{LFS} = (5.2\text{–}6.7) \times 10^{21}$ s^{-1}. As a result, Γ_p^{LFS} is larger than $|\Gamma_p^{HFS}|$, and the LFS-enhanced asymmetry is produced mostly by positive or negative contributions of the drift component. On the other hand, the drift flux at the private flux region, $\Gamma_p^{Prv} = -(3.7\text{–}3.9) \times 10^{21}$ s^{-1}, produces HFS-enhanced asymmetry, and the contribution of Γ_p^{Prv} is larger than Γ_p^{HFS}.

When the detachment occurs at the LFS divertor target, however, Γ_p^{Prv} decreases to zero and $\Gamma_{p,drift}^{LFS}$ changes the direction away from the divertor as mentioned in section 4.1. At the same time, both $|\Gamma_{p,\parallel}^{HFS}|$ and $\Gamma_{p,\parallel}^{LFS}$ increase by a large amount with increasing $\bar{n}_e$, and the parallel components become dominant in the particle transport towards the divertor: $\Gamma_{p,drift}^{HFS}/|\Gamma_{p,\parallel}^{HFS}|$ and $\Gamma_{p,drift}^{LFS}/\Gamma_{p,\parallel}^{LFS}$ are decreased from 12 to 9% and from 28 to 6%, respectively. Here, Γ_p^{LFS} is larger than $|\Gamma_p^{HFS}|$, and the LFS-enhanced asymmetry in the divertor ion flux is caused by the parallel flux components.

4.3. In–out asymmetry in the divertor ion flux

Influences of Γ_p^{HFS}, Γ_p^{LFS} and Γ_p^{Prv} on the in–out asymmetry in the divertor ion flux are discussed. A part of Γ_p^{LFS} is exhausted into the private flux region by diffusion and radial $E_\theta \times B$ drift before reaching the target plate. We make the following assumption that such an ion flux into the private flux region is comparable to $|\Gamma_p^{Prv}|$. Under the assumption, total ion fluxes into the recycling zone of the HFS and LFS divertor are estimated as $\Gamma_p^{HFS} + \Gamma_p^{Prv}$ and $\Gamma_p^{LFS} - |\Gamma_p^{Prv}|$,

Table 1. Poloidal components of parallel ion flux ($\Gamma_{p,\parallel}$), $E_r \times B$ drift flux ($\Gamma_{p,drift}$), and net ion flux ($\Gamma_{p,\parallel} + \Gamma_{p,drift}$), at the HFS SOL and at the LFS just below the X-point. Positive and negative values represent the ion flux towards the HFS and LFS divertors, respectively. The ratio of $\Gamma_{p,drift}/\Gamma_{p,\parallel}$ shows the influence of the $E_r \times B$ drift on the ion flux towards the divertor. $E_r \times B$ drift flux in the private flux region (Γ_p^{Prv}) and ratio of the ion flux onto the HFS divertor ($\Gamma_p^{Prv}/\Gamma_{p,\parallel}^{HFS} + \Gamma_{p,drift}^{HFS}$) are also shown. Values in each frame show the change with increasing $\bar{n}_e$.

							Private flux region	
	$\bar{n}_e$ (10^{19} m^{-3})		$\Gamma_{p,\parallel}$ (10^{21} s^{-1})	$\Gamma_{p,drift}$ (10^{21} s^{-1})	$\Gamma_{p,\parallel} + \Gamma_{p,drift}$ (10^{21} s^{-1})	$\Gamma_{p,drift}/\lvert\Gamma_{p,\parallel}\rvert$	$\Gamma_{p,drift}^{Prv}$ (10^{21} s^{-1})	$\Gamma_{p,drift}^{Prv}/\lvert\Gamma_p^{HFS}\rvert$
Low n_e	1.27–1.68	High-field-side	$-3.0 \sim -4.0$	$0.9 \sim 2.1$	$-1.5 \sim -2.5$	$0.30 \sim 0.50$		
		Low-field-side	$3.5 \sim 4.3$	$1.8 \sim 2.9$	$5.2 \sim 6.7$	$0.45 \sim 0.75$	$-3.7 \sim -3.9$	$1.5 \sim 2.4$
Divertor detached	2.8–3.8	High-field-side	$-13.3 \sim -25.5$	$1.7 \sim 2.3$	$11.6 \sim 23.2$	$0.12 \sim 0.09$		
		Low-field-side	$27.9 \sim 35.2$	$7.8 \sim 2.0$	$20.1 \sim 33.2$	$0.28 \sim 0.06$	<0.3	<0.03

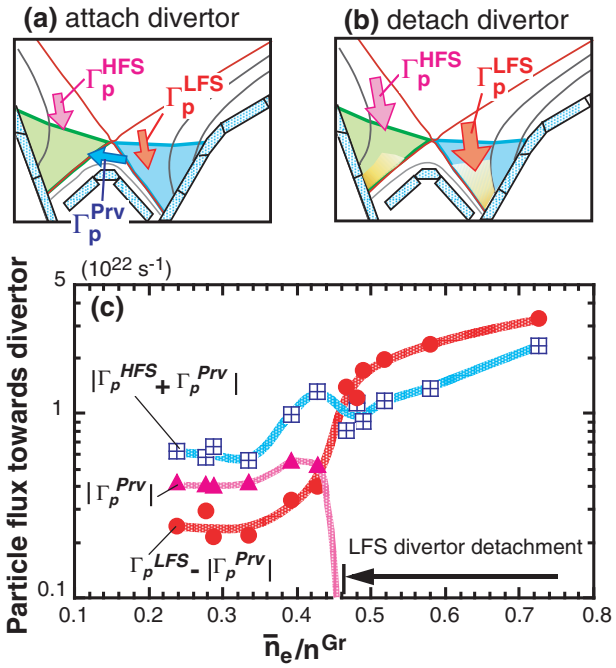

Figure 8. Directions of particle flux are illustrated at the HFS, LFS and private flux region, under (*a*) attached divertor and (*b*) detached divertor conditions. (*c*) Ion fluxes towards the HFS and LFS divertors, $|\Gamma_p^{HFS} + \Gamma_p^{Prv}|$ (⊞) and $\Gamma_p^{LFS} - |\Gamma_p^{Prv}|$ (●), respectively, are shown as a function of $\bar{n}_e/n^{Gr}$. $|\Gamma_p^{Prv}|$ is also shown by ▲.

respectively. $|\Gamma_p^{HFS} + \Gamma_p^{Prv}|$ and $\Gamma_p^{LFS} - |\Gamma_p^{Prv}|$ are shown in figure 8 as a function of $\bar{n}_e/n^{GW}$. For the attached divertor conditions ($\bar{n}_e/n^{GW} = 0.24$–0.45) as illustrated in figure 8(*a*), $|\Gamma_p^{HFS} + \Gamma_p^{Prv}|$ of (5.4–12.6) $\times 10^{21}$ s^{-1} is a factor of 2–3 larger than $\Gamma_p^{LFS} - |\Gamma_p^{Prv}|$ of (2.2–4.4) $\times 10^{21}$ s^{-1}. A large contribution of Γ_p^{Prv} to the HFS-enhanced asymmetry in the divertor ion flux is seen.

When the detachment occurs at the LFS divertor ($\bar{n}_e/n^{GW} > 0.46$) as illustrated in figure 8(*b*), Γ_p^{Prv} disappears and the net particle fluxes towards the HFS and LFS divertors are described as $|\Gamma_p^{HFS}|$ and Γ_p^{LFS}, respectively. These ion fluxes are mostly produced by $\Gamma_{p,\parallel}^{HFS}$ and $\Gamma_{p,\parallel}^{LFS}$, and $\Gamma_{p,\parallel}^{LFS}$ is larger than $\Gamma_{p,\parallel}^{HFS}$. As a result, the in–out asymmetry of the divertor ion flux is reversed, but the asymmetry in Γ_p is small compared to that in the attached divertor: Γ_p^{LFS} becomes a factor of 1.3–1.8 larger than Γ_p^{HFS}.

Similar HFS-enhanced asymmetries in the particle recycling and neutral pressure have been generally observed under the attached divertor. When the divertor detachment occurs such asymmetries become small and reversed. These characteristics of the particle transport in the divertor are determined by changes in Γ_p^{HFS}, Γ_p^{LFS} and Γ_p^{Prv}.

The contributions of drift effects to the particle transport is important for the divertor design and operations in tokamak reactors such as ITER. For the standard operation of the high density plasma ($\bar{n}_e/n^{GW} \sim 0.85$), the divertor detachment is localized near the strike-points and the plasma in the private flux region below the X-point is attached [20]. Thus, $E_r \times B$ drift flow in the private flux region is expected. Particle fluxes into the HFS and LFS divertors would be influenced by the drift, and a study including these drifts will be important to optimize the divertor and pump geometries.

5. Influence of gas puff location on the SOL flow

A technique of the intense gas puff and divertor pump, i.e. 'puff and pump' was demonstrated to exhaust helium and to shield neon argon or carbon ions efficiently from the main plasma [2, 21]. These facts suggested that SOL flow and the plasma profile change during the strong gas puffing into the main SOL. Enhancement of the frictional force on the impurity ions was proposed as a candidate mechanism [3]. However, neither the SOL flow pattern nor the flow velocity has been determined in the experiment.

Influence of the gas puff location on the parallel SOL flow was investigated, for the first time, both for the HFS and LFS SOLs during intense gas puff from the plasma top ('main-puff') and divertor ('divertor-puff') as shown in figure 9. Mach probe locations are downstream and upstream from the main-puff and divertor-puff locations, respectively. At the same time, its influence on the ion fluxes towards the divertor, i.e. Γ_p^{HFS}, Γ_p^{LFS} and Γ_p^{Prv}, is also investigated in order to control the in–out asymmetry in the divertor plasma. Finally, enhancement of the frictional force on the impurity ions during the main gas puffing is evaluated.

The gas puff rate of the main-puff changes from 20 to 60 Pa m^3 s^{-1} ($\Gamma_{puff} = (1.1$–$3.2) \times 10^{22}$ atoms s^{-1}) on a shot-by-shot basis. These values are comparable to or larger than the ion flux towards the divertor. A constant puff rate is

maintained during the measurements, and $\bar{n}_e$ is increased up to 3.3×10^{19} m^{-3} under the attached divertor condition for the main-puff case. In these experiments, the hydrogen L-mode plasma with $I_p = 1.6$ MA, $B_t = 3.3$ T (ion ∇B drift direction towards the divertor) and $P_{NBI} = 4.9$ MW is used.

5.1. SOL flow and ion flux during strong gas puffing

Profiles of $M_\parallel$ and n_e are compared for the main-puff and divertor-puff cases, where $\bar{n}_e$ is comparable $(2.6–2.7) \times 10^{19}$ m^{-3} ($\bar{n}_e/n^{GW} \sim 0.52$). For the main-puff, enhancements of $M_\parallel$ and n_e are observed both at the HFS and LFS, compared to those for the divertor-puff. At the HFS, as shown in figures 10(a) and (b), $M_\parallel$ increases by 20% in the wide region between the separatrix and the outer flux surfaces, and n_e also increases similarly by 20–40%. As a result, the parallel ion flux density ($n_i V_\parallel \Theta$) increases over the wide SOL region as shown in figure 11(a): a maximum increment of 40% is observed at $r_{mid} \sim 15$ and 30 mm. On the other hand, at the LFS SOL near the X-point, figures 10(c) and (d) show that an increase in $M_\parallel$ (<25%) is observed only at $10 < r_{mid} < 20$ mm, and that the n_e profile is comparable. Thus, the small increase in $n_i V_\parallel \Theta$ (maximum increment of 20%) is seen only in the narrow region of the outer flux surfaces ($r_{mid} = 10–15$ mm) as shown in figure 11(b).

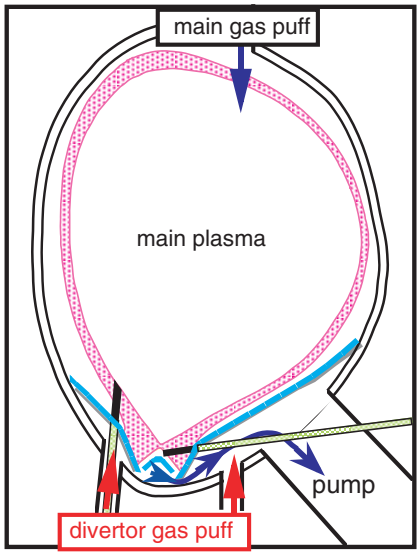

Figure 9. Locations of main gas puff, divertor gas puff and Mach probes.

The total ion flux is compared between the main-puff and the divertor-puff. Γ_p^{HFS} and Γ_p^{LFS} are evaluated from equation (1), and the values are shown in figure 12 as a function of $\bar{n}_e$, where a positive value shows the direction towards the divertor. Horizontal bars show changes in $\bar{n}_e$ during the probe measurement (0.4 s). For relatively high $\bar{n}_e = (2–3) \times 10^{19}$ m^{-3} ($\bar{n}_e/n^{GW} = 0.4–0.6$), parallel SOL flow components, $\Gamma_{p,\parallel}^{HFS}$ and $\Gamma_{p,\parallel}^{LFS}$, are dominant in particle transport: fractions of the drift flux, $\Gamma_{p,drift}^{HFS}/\Gamma_{p,\parallel}^{HFS}$ (~0.2) and $\Gamma_{p,drift}^{LFS}/\Gamma_{p,\parallel}^{LFS}$ (~0.4), are relatively small. For the main-puff, a large enhancement of Γ_p^{HFS} (a factor of 1.4–2) is found at the same $\bar{n}_e$, while Γ_p^{LFS} is 1.1–1.2 times larger. These results suggest that the bulk of the SOL plasma generated by the main-puff is brought towards the HFS divertor.

Since Γ_p^{HFS} is enhanced by the main-puff, the in–out asymmetry in the divertor plasma is determined mostly by Γ_p^{HFS} and Γ_p^{Prv} under the attached divertor condition. The ion fluxes towards the HFS divertor, i.e. Γ_p^{HFS} and Γ_p^{Prv}, are investigated. Figure 13(a) shows that the values of Γ_p^{Prv} are similar ($(8–11) \times 10^{21}$ s^{-1}) for the two gas puff locations and increasing $\bar{n}_e$. The ratios of $\Gamma_p^{HFS}/\Gamma_p^{Prv}$ in figure 13(b) show that Γ_p^{HFS} has a large contribution to the HFS-enhanced asymmetry for the intense main-puff, and that $\Gamma_p^{HFS}/\Gamma_p^{Prv}$ is

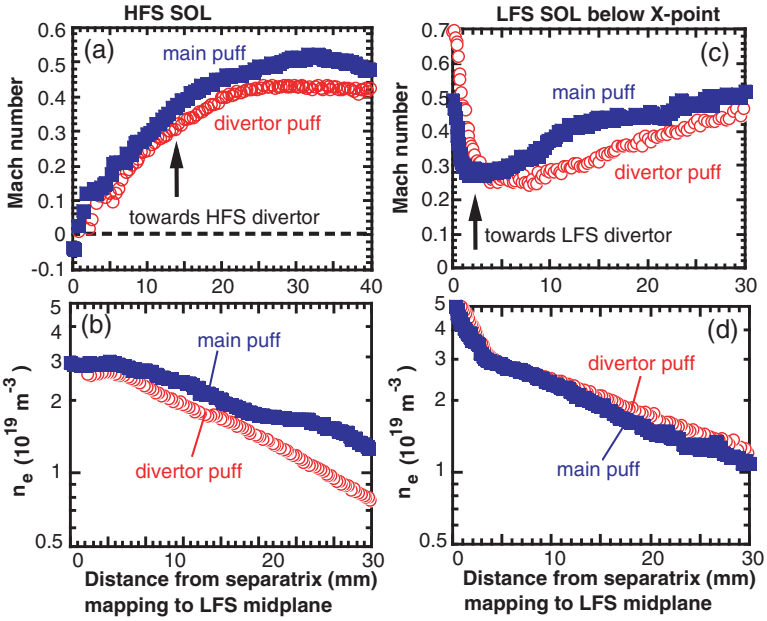

Figure 10. Mach number profiles (a) at the HFS SOL and (c) at LFS just below X-point, for the same $\bar{n}_e = (2.6–2.7) \times 10^{19}$ m^{-3}. Electron density profiles, (b) at the HFS, and (d) the LFS. Squares and circles represent the main and divertor gas puff cases, respectively.

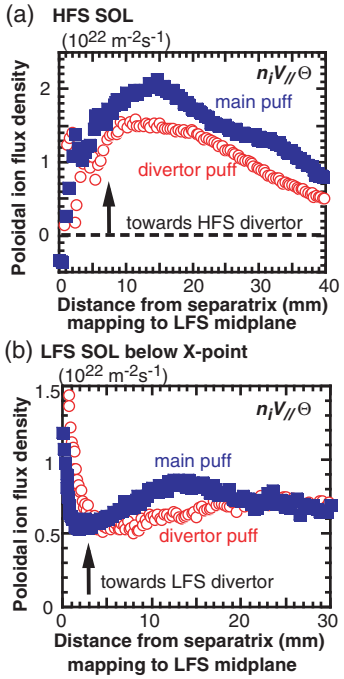

Figure 11. Poloidal components of the parallel ion flux density, $n_i V_{\parallel}\Theta$, (*a*) at the HFS SOL and (*b*) at the LFS just below the X-point. Squares and circles represent the main and divertor gas puff cases, respectively.

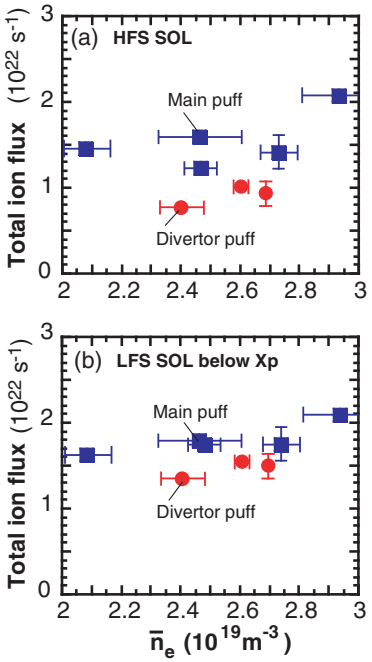

Figure 12. Total ion fluxes (*a*) towards the HFS divertor, and (*b*) towards the LFS divertor, as a function of $\bar{n}_e$. The horizontal bars show the increment of $\bar{n}_e$ during the probe measurement (0.4 s). Squares and circles represent the main and divertor gas puff cases, respectively.

increased with $\bar{n}_e$. On the other hand, for the divertor-puff, Γ_p^{Prv} is larger than or comparable to Γ_p^{HFS}. The fact that $\Gamma_p^{HFS} < \Gamma_p^{Prv}$ was also observed for the main puff using feedback control to maintain constant values of $\bar{n}_e$ as shown in sections 3

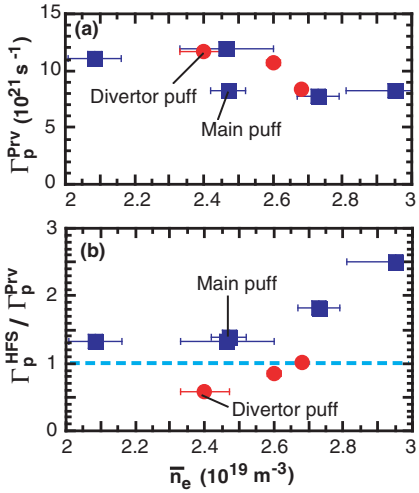

Figure 13. (*a*) Total drift flux at the private flux region, Γ_p^{Prv} and (*b*) ratios of total poloidal fluxes towards the HFS divertors to the total drift flux at the private flux region, $\Gamma_p^{HFS}/\Gamma_p^{Prv}$, as a function of $\bar{n}_e$. Squares and circles represent values at the HFS and LFS SOL.

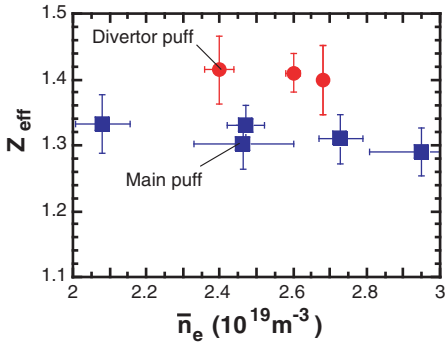

Figure 14. Z_{eff} during the main gas puff (■) and divertor gas puff (●), as a function of $\bar{n}_e$.

and 4, where the deuterium gas puff rate was relatively small, i.e. (2.7–10) × 10^{21} atoms s^{-1}. As a result, the HFS-enhanced asymmetry of the ion flux can be enhanced using the intense main-puff.

5.2. *Effect of the SOL flow on impurity shielding*

A reduction of Z_{eff} (the main contribution of carbon ions) during the strong main puff is demonstrated as shown in figure 14. Before the strong gas puff, Z_{eff} is 1.47–1.53 at low $\bar{n}_e$ = (1.6–1.8) × 10^{19} m^{-3} with the gas puff rate of 3–8 Pa m^3 s^{-1}. During the strong main-puff with the gas puff rate of 20–40 Pa m^3 s^{-1} (Γ_{puff} = (1.1–2.1) × 10^{22} atoms s^{-1}), Z_{eff} is reduced largely to 1.29–1.33, compared to 1.40–1.43 for the divertor-puff. The carbon concentration in the main plasma (evaluated from the CVI line brightness), n_C/n_e, also decreases from 1.5% to 0.7–0.8% for the main-puff compared to 1.1–1.2% for the the divertor-puff.

The large increments in Γ_p^{HFS} suggest that the difference in the impurity reduction is caused by enhancement of the SOL flow and electron density at the HFS. The *friction* and *thermal*

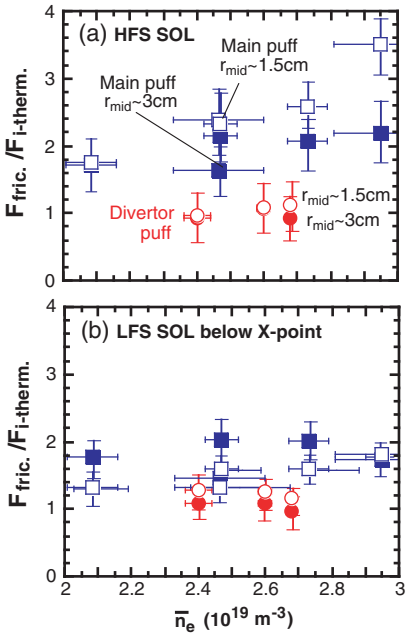

Figure 15. Ratios of $F_{\rm fric}/F_{\rm i\text{-}therm}$, at the outer flux surfaces, i.e. $r_{\rm mid} = 1.5$ (open symbols) and $r_{\rm mid} = 3$ cm (closed symbols), during the main gas puff (squares) and divertor gas puff (circles), as a function of $\bar{n}_{\rm e}$: (*a*) at the HFS SOL, and (*b*) at the LFS SOL just below the X-point.

forces of bulk ions on impurity ions are estimated [22] from

$$F_{\rm fric} = (v_{\rm imp} - v_{\rm i})\tau_{\rm imp}^{-1} \sim 1.6 \times 10^3 Z^2 n_{\rm i} M_{\parallel} T_{\rm i}^{-1} \quad [\mathrm{eV\,m^{-1}},\ 10^{19}\,\mathrm{m^{-3}}, \mathrm{eV}] \qquad (2)$$

and

$$F_{\rm i\text{-}therm} = \beta \nabla_{\parallel} T_{\rm i} \sim 2.2 Z^2 \nabla_{\parallel} T_{\rm i}\ [\mathrm{eV\,m^{-1}},\ \mathrm{eV}], \qquad (3)$$

respectively. Enhancement of $F_{\rm fric}$ is defined by the ratio of $F_{\rm fric}/F_{\rm i\text{-}therm}$, and the values at the outer flux surfaces are shown in figure 15 as a function of $\bar{n}_{\rm e}$. $M_{\parallel}$ and $n_{\rm e}$ are measured with the HFS and X-point Mach probes. Here, $Z = 3$, $n_{\rm i} = n_{\rm e}$, and $T_{\rm i}$ and $\nabla_{\parallel} T_{\rm i}$ are calculated from the UEDGE simulation results. During the strong main-puff, $F_{\rm fric}/F_{\rm i\text{-}therm}$ at the HFS SOL is increased to 1.8–2 (at $r_{\rm mid} = 1.5$ cm) and 1.8–3.5 (at $r_{\rm mid} = 3$ cm), since both $n_{\rm i}$ and $M_{\parallel}$ are increased. On the other hand, $F_{\rm fric}/F_{\rm i\text{-}therm}$ is 0.9–1.0 for the divertor-puff; i.e. the two forces are balanced. At the LFS SOL, $F_{\rm fric}/F_{\rm i\text{-}therm}$ stays at 0.9–1.5 both for the main-puff and divertor-puff, except near $r_{\rm mid} = 15$ mm.

As a result, enhancement of $F_{\rm fric}$ during the intense main-puff was found to be 2–3.5 times larger than $F_{\rm i\text{-}therm}$ at the HFS, while $F_{\rm fric}$ and $F_{\rm i\text{-}therm}$ at the LFS divertor entrance are comparable both for the main-puff and the divertor-puff. This result suggests that reductions of $Z_{\rm eff}$ and $n_{\rm C}/n_{\rm e}$ are produced by improvement of the impurity shielding at the HFS SOL.

6. Summary and conclusions

Measurements of the SOL flow in the JT-60U tokamak, and application of UEDGE simulation revealed the plasma flow pattern in the main SOL and the effect of the plasma drifts on the SOL flow. Reversal of parallel SOL flow at the HFS and LFS SOLs, and in–out asymmetry in the flow pattern were distinguished by the three Mach probe measurements. They were qualitatively consistent with UEDGE simulation including drift effects. It was found that stagnation of the parallel SOL flow appears near the X-point of the HFS and LFS SOLs as well as at the plasma top. The subsonic level of the Mach numbers in the measurements ($M_{\parallel} = 0.4$–0.5) at the LFS SOL and the outer flux surfaces of the HFS SOL was generally larger than that of simulations. The difference between the measurements and simulations was not understood in this study of drift modelling.

Particle fluxes produced by the parallel and drift flows were investigated from the measured $M_{\parallel}$, $n_{\rm e}$ and E_r profiles both at the HFS and LFS SOLs for the ion ∇B drift direction towards the divertor. The contribution of the $E_r \times B$ drift flux to the net particle transport in the main SOL was large at relatively low density, i.e. $\Gamma_{\rm p,drift}/\Gamma_{\rm p,\parallel}$ is 30–50% (HFS SOL) and 45–75% (LFS SOL). On the other hand, evaluations of total ion fluxes onto the HFS divertor, i.e. $\Gamma_{\rm p}^{\rm Prv}/\Gamma_{\rm p}^{\rm HFS} = 1.5$–$2.4$, confirmed that the $E_r \times B$ drift flux in the private region plays the most important role for producing HFS-enhanced asymmetry in the divertor ion flux under the attached divertor condition.

Influences of the gas puff location and the puff rate on the particle flux towards the divertor were distinguished. The parallel SOL flow towards the divertor was increased with the intense main-puff, and the dominant effects on the SOL flow, density and *friction force* appear, in particular, at the HFS SOL. This result was consistent with the conventional model of reduction in $Z_{\rm eff}$: the shielding effect by the *friction force* from the SOL flow is enhanced at the HFS SOL and divertor.

For the high density plasma in a tokamak reactor such as ITER, the divertor detachment is localized near the strike-points and the attached plasma will exist in the private flux region. Under such a condition as shown in the attached divertor in section 6, particle fluxes onto the HFS and LFS divertors will be influenced by the drifts. Improvements of simulation including drift effects and of the plasma and impurity modelling would be necessary for design work to optimize the divertor and pump geometries.

Acknowledgments

The authors would like to thank the JT-60U team, and especially Mr K. Masaki and Facilities Division II for helping in the installation of the inner reciprocating Mach probe. They also thank Dr O. Naito for equilibrium mapping, Dr A. Chankin for helpful discussions, and Dr R. Yoshino for encouragement in this research.
Work by LLNL performed under auspices of US DOE under contract No. W-7405-Eng-48.

References

[1] Stangeby P.C. and McCracken G.M. 1990 *Nucl. Fusion* **30** 1225
[2] Mahdavi M.A. *et al* 1995 *J. Nucl. Mater.* **220–222** 13
[3] Shimizu K., Takizuka T. and Sakasai A. 1997 *J. Nucl. Mater.* **241–243** 167
[4] Loarte A. *et al* 1993 *Proc. 20th Eur. Conf. on Control. Fusion and Plasma Physics* vol 17C (Lisboa: EPS) p 555
[5] Pitcher C.S. *et al* 1993 *Proc. 20th Eur. Conf. on Control. Fusion and Plasma Physics* vol 17C (Lisboa: EPS) p 291

[6] LaBombard B. *et al* 1997 *J. Nucl. Mater.* **241–243** 149
[7] Asakura N. *et al* 1999 *Nucl. Fusion* **39** 1983
[8] Chankin A.V. and Stangeby P.C. 1994 *Plasma Phys. Control. Fusion* **36** 1485
[9] Chankin A.V. and Stangeby P.C. 2003 *Proc. 30th Eur. Conf. on Control. Fusion and Plasma Physics* (St Petersburg: EPS) O-4.1C
[10] Porter G.D. *et al* 2003 *J. Nucl. Mater.* **313–316** 1085
[11] Asakura N. *et al* 2000 *Phys. Rev. Lett.* **84** 3093
[12] Rognlien T.D., Porter G.D. and Ryutov D.D. 1999 *J. Nucl. Mater.* **266–269** 654
[13] Boedo J.A. *et al* 2000 *Phys. Plasma* **7** 1075
[14] Hutchinson I.H. 1988 *Phys. Rev.* A **37** 4358
[15] Asakura N. *et al* 2002 *Plasma Phys. Control. Fusion* **44** 2101
[16] Stangeby P.C. and Chankin A.V. 1996 *Nucl. Fusion* **36** 839
[17] Chankin A.V. and Stangeby P.C. 1996 *Plasma Phys. Control. Fusion* **38** 1879
[18] Porter G.D. *et al* 2000 *Phys. Plasma* **7** 3663
[19] Asakura N. *et al* 2003 *J. Nucl. Mater.* **313–316** 820
[20] Kukushkin A.S. *et al* 2001 *J. Nucl. Mater.* **290–293** 887
[21] Hosogane N. *et al* 1999 *J. Nucl. Mater.* **266–269** 296
[22] Neuhauser J. *et al* 1984 *Nucl. Fusion* **24** 39